ORIGINAL ARTICLE

Effect of adding titanium on corrosion and wear resistance of $Al_{0.7}CoCrFeNiTi_x$ high entropy alloy

Mariusz Walczak · Wojciech J. Nowak · David Vališ · Wojciech Okuniewski · Dariusz Chocyk · Kamil Pasierbiewicz

Received: 20 March 2026 / Revised: 10 August 2026 / Accepted: 13 August 2026
© The Author(s) 2026

Abstract
High-entropy alloys based on the Al-Co-Cr-Fe-Ni system are considered promising materials for applications exposed to wear and corrosive environments. In this study, the effect of titanium addition on the microstructure, mechanical properties, tribological performance and corrosion behaviour of $Al_{0.7}CoCrFeNiTi_x$ alloys (x = 0, 0.05, 0.2 and 0.5) produced by arc melting was investigated and compared with AISI 304L stainless steel. Microstructural analyses revealed a gradual evolution from a lamellar Widmanstätten morphology to a more complex multiphase structure with an increasing fraction of BCC/B2 phases and enhanced chemical segregation between Al–Ti–rich and Fe–Cr-rich regions. At the highest Ti content, additional intermetallic phases such as Ni_3Ti and σ were identified. Increasing Ti content significantly improved hardness and nanoindentation parameters (H/E and H^3/E^2), indicating enhanced resistance to plastic deformation under contact loading. Sliding tests performed in 3.5 wt.% NaCl solution showed that the $Al_{0.7}CoCrFeNiTi_{0.2}$ alloy exhibited the lowest wear factor, approximately 54% lower than that of the Ti-free alloy. The wear behaviour was dominated by abrasive and oxidative mechanisms. Electrochemical measurements indicated that Ti addition reduced the corrosion current density and improved passivation behaviour, while the highest pitting resistance was obtained for the Ti0.2 composition. Localized corrosion preferentially initiated in Al–Ni-rich regions depleted in Cr. Overall, the results indicate that the $Al_{0.7}CoCrFeNiTi_{0.2}$ alloy provides the most favourable combination of mechanical, tribological and corrosion properties in chloride-containing environments.

Keywords High entropy alloy · Ti addition · Wear · Nanoindentation · Corrosion

1 Introduction

In the last decade, high-entropy alloys (HEAs) have shown significant progress in the development of functional and structural materials due to their enormous potential in terms of performance and service properties. Numerous studies have demonstrated that individual HEAs exhibit high hardness and strength, excellent oxidation resistance [1], resistance to abrasive and cavitation wear [2], as well as good corrosion resistance [3]. These characteristics make them promising candidates for replacing conventional materials such as austenitic stainless steels in many applications, thereby significantly expanding the range of their potential use.

Published online: 07 September 2026

Among the many possible alloy systems, HEAs based on the Al-Co-Cr-Fe-Ni composition attract particular attention due to their wide spectrum of potential applications, including operation in flow environments exposed to both wear and corrosion. Interest in this alloy system arises primarily from the possibility of tailoring structural properties depending on the aluminum content. For $Al_xCoCrFeNi$ alloys, it has been established that increasing the Al content (in molar ratio) induces a phase transformation from FCC (Face-Centred Cubic) to BCC (Body-Centred Cubic). For compositions with $x \leq 0.4$, HEAs exhibit a single-phase FCC structure. In the range of $0.5 \leq x \leq 0.9$, the alloys show a mixed FCC and BCC structure, whereas for $x > 0.9$ a single BCC phase is observed [4].

According to the literature [5, 6], the BCC phase is characterized by lower tensile ductility but higher strength compared with the FCC phase. The increase in hardness and strength associated with higher Al content results from the fact that the atomic radius of Al is larger than that of the other constituent elements in the HEA, which leads to increased lattice distortion [7].

Corrosion studies of $Al_xCoCrFeNi$ alloys (x = 0.3, 0.5 and 0.7) conducted by Shi et al. [8] showed that alloys with a single FCC phase exhibit higher corrosion resistance compared with dual-phase FCC + BCC structures. For the Al0.3 composition, only sparsely distributed corrosion pits were observed and the alloy showed the highest corrosion resistance. In contrast, for the Al0.5 and Al0.7 alloys, pitting corrosion associated with micro-galvanic effects occurred in the BCC phase regions enriched in Al and Ni and depleted in Cr. Increasing the Al content resulted in a decrease in pitting potential and an increase in corrosion current density. Similarly, experimental studies by Kao et al. [9] demonstrated that Al reduces corrosion resistance in H_2SO_4 due to the porous and relatively weak passive Al_2O_3 film formed on $Al_xCoCrFeNi$ alloys (x = 0, 0.25, 0.5 and 1). Studies by Nair et al. [10] also reported higher corrosion resistance for equiatomic $Al_xCoCrFeNi$ alloys with an FCC structure (x = 0.1, 1 and 3). In that work, an increase in corrosion current density was observed with increasing Al content, indicating poorer corrosion resistance of the BCC phase. However, investigations of other degradation mechanisms such as slurry erosion–corrosion, liquid impingement erosion and sliding wear showed more favourable performance for HEAs with a BCC structure. Furthermore, all tests (except corrosion) demonstrated higher resistance to various forms of wear for $Al_xCoCrFeNi$ alloys compared with AISI 316L stainless steel. It is worth noting that the literature reports both improved corrosion resistance of Al-Co-Cr-Fe-Ni HEAs compared with austenitic stainless steels [8–10] as well as cases where lower corrosion resistance has been observed [1, 2, 11]. When comparing the corrosion behaviour of HEAs and stainless steels, it is therefore important to consider factors such as the manufacturing method and whether the material is produced as a bulk alloy or as a coating.

Another research direction in the development of Al-Co-Cr-Fe-Ni alloys involves the addition of various alloying elements at different molar concentrations to tailor their properties. The literature reports attempts to incorporate elements such as Si (improved wear resistance) [3], Nb (enhanced mechanical properties) [12], V (improved wear resistance) [13], B (improved magnetic properties) [14], Zr (enhanced mechanical properties) [15], Cu (improved compressive strength) [16], Mn (improved mechanical and corrosion properties) [17], Mo (improved wear resistance in flow environments) [18], and Ti (increased hardness and wear resistance) [19]. Recent investigations [20] have also highlighted the important role of processing conditions and microstructural evolution in determining the mechanical and tribological behaviour of high-entropy alloys and their coatings.

An interesting approach is the incorporation of Ti into the equimolar $AlCoCrFeNiTi_x$ HEA coating system (x = 0, 0.25, 0.5, 0.75 and 1) reported by Yue et al. [21]. In that study, increasing Ti content led to higher hardness attributed to solid-solution strengthening. However, improvement in corrosion resistance was observed only up to Ti0.5, whereas further increases in Ti resulted in higher corrosion current density. Although Ti promotes the formation of a protective TiO_2 layer, when the Ti content exceeded 0.5 mol in the coating, the formation of Laves phases and structural defects reduced the corrosion resistance of the HEA coatings. Similarly, Zhang et al. [22] investigated the corrosion resistance of $Al_xCoCrFeNiTi_{0.5}$ alloys (x = 0, 0.5 and 1). The most favourable behaviour was observed for $Al_{0.5}CoCrFeNiTi_{0.5}$, which exhibited a mixed FCC + BCC structure. Literature data are also available regarding the effect of Ti addition (0.5 mol) on the tribological behaviour of equimolar AlCoCrFeNi alloys with a BCC structure [19, 23] under dry sliding conditions and air flow, where improved

wear resistance was reported. In addition, tribological and corrosion tests of equimolar AlCoCrFeNiTi coatings demonstrated improved wear resistance due to oxidative wear mechanisms and enhanced corrosion resistance associated with increased passivation of the coatings [24].

Although Ti-modified HEAs generally exhibit significantly improved wear and corrosion resistance compared with their reference compositions, their behaviour in flow environments containing chloride ions has not yet been fully clarified. Recent studies do not provide a clear trend regarding the optimal Ti content in HEAs intended for applications in such environments. Therefore, determining the appropriate Ti content for mixed FCC + BCC high-entropy alloys in relation to their resistance to various forms of wear remains an important issue. Based on the above considerations concerning the properties of Al-Co-Cr-Fe-Ni based HEAs with different phase compositions (FCC and BCC), as well as the available data regarding the influence of Ti addition, the present work aims to analyse the corrosion and tribological behaviour of Al0.7CoCrFeNiTix alloys. For this specific alloy composition, only our previous studies [25] concerning structural properties and solid particle erosion resistance have been reported so far. In contrast, the influence of Ti addition on the tribological behaviour and corrosion resistance of $Al_{0.7}CoCrFeNiTi_x$ alloys in 3.5 wt.% NaCl solution has not yet been investigated and therefore represents a novel contribution of the present work.

2 Experimental procedure

2.1 Materials and methods

The subject of the study was $Al_{0.7}CoCrFeNiTi_x$ HEA alloys (where $x = 0$, 0.05, 0.2, and 0.5 in molar ratio), whose properties were compared with those of AISI 304L austenitic stainless steel. Pure elemental powders (purity 99.99 wt.%) were used for the preparation of the HEA alloy compositions. The nominal and experimentally obtained chemical compositions of the HEAs are presented in Table 1. Elemental powders of Al, Co, Cr, Fe, Ni, and Ti were first mechanically mixed in a ball mill for 2 h under an argon atmosphere (5N purity). The powder mixtures were then cold-pressed using a hydraulic press to obtain cylindrical compacts with a diameter of 15 mm and a height of approximately 15 mm. The compacts were subsequently remelted in an arc-melting furnace (Arc-Melter, Edmund Bühler GmbH) under an argon atmosphere. Each sample was remelted five times to improve chemical homogeneity. Figure 1a shows the overview of the sample located in the vacuum chamber just after remelting process, while Fig. 1b exhibits the macropicture of HEA in the as cast conditions. One can clearly see that the sample after 5 times remelting is free from pores or other casting defects (especially Fig. 1b). The samples were investigated in the as-cast condition. The chemical compositions of the studied HEA alloys were designed based on thermodynamic calculations performed using the CALPHAD method and are described in detail in [25]. In this study, the surfaces of the as-cast HEA samples used for all experimental tests were prepared following the same procedure. Initially, the samples were ground using Tissediam diamond grinding discs (Presi, France) with

Table 1 Predicted and measured chemical composition of the investigated $Al_{0.7}CoCrFeNiTi_x$ alloys

Elements (at. %)	Co	Ni	Al	Cr	Fe	Ti	Specimen
Predicted							
	21.3	21.3	14.9	21.3	21.3	–	$Al_{0.7}CoCrFeNi$
	21.0	21.0	14.7	21.0	21.0	1.0	$Al_{0.7}CoCrFeNiTi_{0.05}$
	20.4	20.4	14.3	20.4	20.4	4.1	$Al_{0.7}CoCrFeNiTi_{0.2}$
	19.2	19.2	13.5	19.2	19.2	9.6	$Al_{0.7}CoCrFeNiTi_{0.5}$
Measured							
	21.1	21.4	13.5	22.1	21.9	–	$Al_{0.7}CoCrFeNi$
	19.8	21.3	13.2	22.5	21.9	1.3	$Al_{0.7}CoCrFeNiTi_{0.05}$
	19.1	20.8	12.8	21.6	21.3	4.5	$Al_{0.7}CoCrFeNiTi_{0.2}$
	21.5	18.6	11.8	19.1	19.0	10.0	$Al_{0.7}CoCrFeNiTi_{0.5}$



Fig. 1 Pictures showing: **a** overview of the samples just after remelting process in vacuum chamber and **b** macropicture of HEA in the as cast conditions

successive grit sizes of 125, 75, and 40 µm on a metallographic grinding and polishing machine (Buehler, Beta). Subsequently, the samples were wet-ground using 2500-grit SiC abrasive paper and then polished using diamond suspensions with particle sizes of 3 µm, followed by a final polishing step with a 1 µm suspension.

2.2 Microstructure analysis

The X-ray diffraction (XRD) pattern was used to phase identify, the crystallite size determination and strain analysis of $Al_{0.7}CoCrFeNiTi_x$ samples. XRD measurements were performed in Bragg–Brentano geometry (θ-2θ), using the high-resolution diffractometer (Empyrean Panalytical, Almelo, The Netherlands). The profiles were recorded using CuK_α (l = 1.5418 Å) radiation with Ni β filter (to suppress CuK_β radiation) and collected over the range $2\theta = 20 \div 100°$ with the step size $2\theta = 0.01°$and counting time 6 s per data point. The fixed divergence slit of 0.5° was used together with the beam mask of 5 mm and all scans were carried out in continuous mode. Incident and receiving Soller's slits were 0.04 rad. The crystalline phase in the samples was identified using High Score Plus software package with Crystallography Open Database. Based on the position and full-width half maximum (FWHM) of corresponding peaks, Williamsons-Hall plot (W–H plot) method were adopted to calculate the crystallite size and its corresponding micro-strain in each sample.

The microstructure analysis was performed using a scanning electron microscope Phenom ProX scanning electron microscope (Phenom-World, USA) with EDS (Energy Dispersive X-ray Spectroscopy) detector.

2.3 Hardness and nanoindentation testing

The surface hardness of the investigated alloys was measured using a Vickers microhardness tester FM-800 (Future-Tech Corp., Japan) equipped with the ARS 900 automatic measurement system. The measurements were performed under a load of 9.807 N (HV_1) with a dwell time of 15 s. For each batch of samples, 15 indentations were carried out at different locations on the sample surface, and the reported hardness values represent the arithmetic mean of the measurements.

Subsequently, nanoindentation tests were performed using the Oliver–Pharr method [26] in accordance with PN-EN ISO 14577–1 [27] employing an ultra-nanoindentation tester (UNHT, Anton Paar). A diamond Berkovich indenter was used for all measurements. Before testing, the indenter area function and frame compliance were calibrated using a fused silica reference sample in accordance with ISO 14577–1. The load was applied at a constant loading rate of 20 mN/min from the initial contact between the indenter and the sample surface until the maximum load (F_{max}) was reached. Contact detection was defined by a stiffness threshold exceeding 150 µN/µm. The maximum load was maintained for 10 s, followed by unloading at a constant rate of 20 mN/min.

During the nanoindentation tests, the applied load (F) and the indenter penetration depth (h) were continuously recorded. For each sample, 100 indentations arranged in a 10 × 10 matrix were performed using a maximum load F_{max} of 10 mN. Outliers were excluded from the analysis using a standard statistical criterion, and the reported values represent the mean of the valid measurements. In addition to the standard mechanical parameters obtained from nanoindentation tests, including hardness (H), elastic modulus (E), the H/E ratio (elastic strain to failure), H^3/E^2 (plastic resistance), elastic recovery index (ERI), and plasticity index (PI), the total work performed by the indenter was also evaluated according to Eq. (1):

$$W_{\text{total}} = W_{\text{elast}} + W_{\text{plast}} \tag{1}$$

where W_{elast} and W_{plast} denote the elastic and plastic deformation energies, respectively, determined from the areas under the loading–unloading curves.

The elastic recovery index (ERI) and plasticity index (PI) were calculated using Eqs. (2) and (3), respectively:

$$ERI = \frac{W_{\text{elast}}}{W_{\text{total}}} \tag{2}$$

$$PI = \frac{W_{\text{plast}}}{W_{\text{total}}} \tag{3}$$

2.4 Electrochemical measurements

Electrochemical measurements of the investigated materials were carried out in a 3.5 wt.% NaCl aqueous solution at ambient temperature (~22 °C). The electrochemical behavior was evaluated using a conventional three-electrode cell configuration, consisting of the tested sample used as the working electrode (exposed surface area of 0.5 cm^2), a platinum plate as the counter electrode, and a saturated calomel electrode (SCE) as the reference electrode. Electrochemical tests were performed using an ATLAS 0531 Electrochemical Unit & Impedance Analyser (Atlas Solich). To ensure stabilization of the open circuit potential, the samples were immersed in the electrolyte for 60 min prior to the measurements. Potentiodynamic polarization curves were recorded with an automatic potential scan rate of 1 mV/s in the potential range from −0.6 V to +0.6 V vs. SCE. For each material, corrosion measurements were performed in triplicate to ensure the reproducibility and reliability of the results. The electrochemical measurement data were analyzed using AtlasCorr software. Corrosion parameters, including the corrosion current density (i_{corr}) and corrosion potential (E_{corr}), were determined from the Tafel extrapolation method of the potentiodynamic polarization curves using AtlasLab software. The surfaces after the corrosion tests were examined using a scanning electron microscope Phenom ProX (Phenom-World, USA) equipped with an energy-dispersive X-ray spectroscopy (EDS) detector.

2.5 Wear testing

Sliding wear tests were conducted in a 3.5 wt.% NaCl aqueous solution at room temperature using a ball-on-disc tribometer (CSM Instruments, Switzerland). Alumina (Al_2O_3) counterbodies (grade G5) with a diameter of 6 mm and a hardness of 1680 HV_1 were employed. The experiments were performed under a normal load of 10 N, a linear sliding speed of 1.88 cm s^{-1}, and a wear track radius of 3 mm. For each condition, three independent tests were carried out. The total sliding distance was 200 m, and the evolution of the coefficient of friction (COF) was recorded continuously throughout the test. The wear rate was quantified using the wear factor (K), calculated according to the Archard [28] equation (Eq. 4):

$$K = \frac{V}{F \cdot s} \left[\text{mm}^3\text{N}^{-1}\text{m}^{-1}\right] \tag{4}$$

where V is the wear volume, F the applied normal load, and s the sliding distance.

The wear volume was determined from the cross-sectional profile of the wear track measured by contact stylus profilometry (Dektak 150, Veeco Instruments, USA) equipped with a 2 µm radius stylus and a loading force of 3 mg. Wear tests were performed on three independent specimens for each material. For each wear track, twelve cross-sectional profiles were recorded at different locations along the wear-track circumference, resulting in a total of 36 profile measurements per material. The acquired profiles were analyzed using the dedicated Dektak software. The wear volume was calculated from the average cross-sectional area of the wear track and the corresponding wear-track circumference. The wear track morphology and chemical composition were examined by SEM–EDS analysis.

3 Results and discussion

3.1 Microstructural characterization

Figure 2 shows the X-ray diffraction patterns of HEA samples. A clear difference can be observed between the diffraction patterns of $Al_{0.7}CoCrFeNi$, $Al_{0.7}CoCrFeNiTi_{0.05,}$ and $Al_{0.7}CoCrFeNiTi_{0.2}$ when compared with the profile of $Al_{0.7}CoCrFeNiTi_{0.5}$. These patterns exhibit diffraction peaks located at approximately 2θ = 30.9°, 43,5°, 44.1°, 51.7°, 64.4°, 74.6°, 81.6° and 90.5°, with noticeable differences in their relative intensities. Analysis revealed that the peak observed in these XRD profiles corresponds to two phases: FCC with the cubic structure and the space group Fm-3 m, and B2/BCC with the cubic structure and the space group Im-3 m. In the profile of the $Al_{0.7}CoCrFeNi$ sample, the highest intensities are observed at 2θ = 43.5° and 51.7°, indicating a significant contribution from the FCC phase. The identified phase constitution is consistent with the results reported by Liu et al. [5] for arc-melted $Al_{0.7}CoCrFeNi$ alloys, which also showed XRD analysis confirming a dual-phase FCC + B2/BCC structure.

The addition of Ti0.05 to the sample increases the B2/BCC phase fraction, as reflected by increased intensities of the peaks at 2θ = 30.9° and 64.4°. In turn, increasing the content to Ti0.2 causes a decrease in the ordered phase relative to the BCC disordered phase, as evidenced by the decreased peak intensities at 2θ = 30.9° and 64.4° and the significant broadening of the peaks at 2θ = 44.9°, 64.4°, and 81.6°. Increasing the Ti content to 0.5 results in

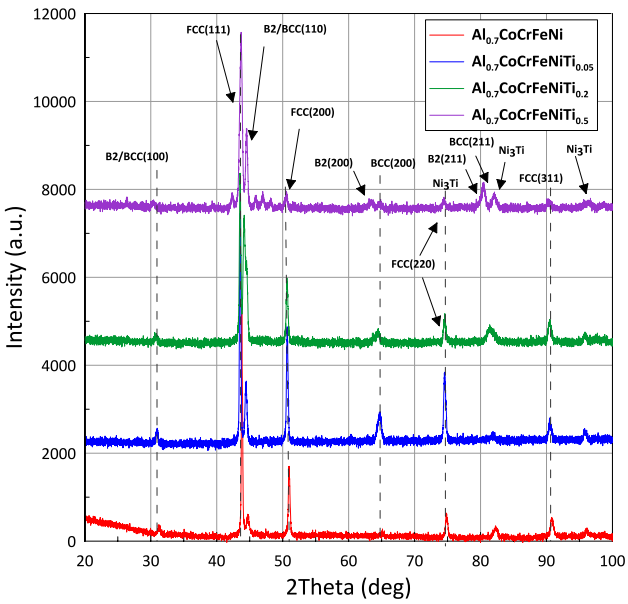


Fig. 2 X-ray diffraction patterns of HEAs

Table 2 The quantitative proportions of individual phases

Sample	FCC (%)	B2/BCC (%)	A2/BCC (%)
$Al_{0.7}CoCrFeNi$	81.9	17.9	0.3
$Al_{0.7}CoCrFeNiTi_{0.05}$	73.8	18.6	7.6
$Al_{0.7}CoCrFeNiTi_{0.2}$	69.0	13.6	17.4
$Al_{0.7}CoCrFeNiTi_{0.5}$	67.9	12.4	19.4

Table 3 The crystallite size and micro-strains

Sample	Crystallite size (nm)	Micro-strains (%)
$Al_{0.7}CoCrFeNi$	46.9	0.06
$Al_{0.7}CoCrFeNiTi_{0.05}$	32.1	0.07
$Al_{0.7}CoCrFeNiTi_{0.2}$	34.1	0.16
$Al_{0.7}CoCrFeNiTi_{0.5}$	32.1	0.16

a clear separation of the peaks at 2θ = 64.4° and 81.6°, and a significant reduction in the peak at 2θ = 30.9°. This indicates the disappearance of the ordered phase B2 and the growth of the disordered phase BCC.

The above results indicate that Ti atom content causes significant changes in the structure. Increasing the Ti content reduces the FCC phase. However, the effect of Ti on the B2/BCC phase is more complex. For smaller Ti contents, the proportion of the ordered B2 phase is greater, and then, as Ti increases, its proportion decreases at the expense of the disordered BCC phase. The two phases exhibit different lattice parameters. To verify the preliminary analysis, a Rietveld analysis was performed. The following phases were included in the analysis: Fm-3 m, Im-3 m, and Pm-3 m. For the sample with the highest Ti content, the P63/mmc and P42/mnm. structures were also considered. The share of these phases was small. Their occurrence is evidenced by peaks at 74.4°, 82.3°, and 96.3°, which are identified as Ni_3Ti phases in the alloy Al0.7CoCrFeNiTi0.5. However, a few other peaks at 2θ = 42.33°, 45.89°, 46.95°, 48.12°, and 49.48° correspond to the σ-phase, which has a tetragonal crystal structure and the space group P42/mnm. This analysis allowed us to determine the quantitative proportions of the phases present in individual samples. Detailed data on the percentage of main phases in individual samples are presented in Table 2. The individual phases are marked at the diffraction peaks in Fig. 2.

To determine the average crystallite size and micro-strain from the broadening of the diffraction peaks in the XRD patterns, the Williamson-Hall method was used. In this method, it is assumed that the total broadening of the diffraction peaks is the sum of the broadenings due to crystallite size distribution and micro-strains. The average crystallite size and micro-strain can be calculated using the Williamson-Hall equation (Eq. 5):

$$\beta \cos(\theta) = \frac{K\lambda}{D} + 4\sin(\theta)\varepsilon \tag{5}$$

where, θ is the diffraction angle, λ is the wavelength of X-ray (λ= 1.5418 Å), K is the Scherrer constant, which generally is taken as 0.9. D is the crystallite size, and ε is the micro strain. The β is the diffraction peak's full width at half maximum (FWHM) in radians, corrected for the instrument's FWHM. The instrument FWHM was determined using a Si reference sample. After measuring the β of some diffraction peaks, the dependence of $\beta\cos(\theta)$ vs. $4\sin(\theta)$ was fitted linearly by the least squares method. The slope of the straight line is the micro-strain, and the intercept of the fitted straight line on the ordinate was used to calculate the crystallite size. Detailed data on average crystallite size and microstrain of HEA samples are summarized in Table 3.

As shown, adding Ti results in a significant reduction in crystallite size. This reduction can be attributed to the formation of the B2/BCC phase. However, in the case of micro-strain, the situation is not so clear. A significant increase in micro-strain is observed for Ti0.2 and is attributed to the increased B2/BCC phase content. In the Al0.7CoCrFeNiTi0.5 sample, maintaining the micro-strain also leads to the formation of the sigma phase.

Figure 3 presents the SEM (BSE) microstructures of the as-cast $Al_{0.7}CoCrFeNiTi_x$ (x = 0, 0.05, 0.2, 0.5) high-entropy alloys. At the same time, Table 4 summarizes the EDS point analysis results obtained from the

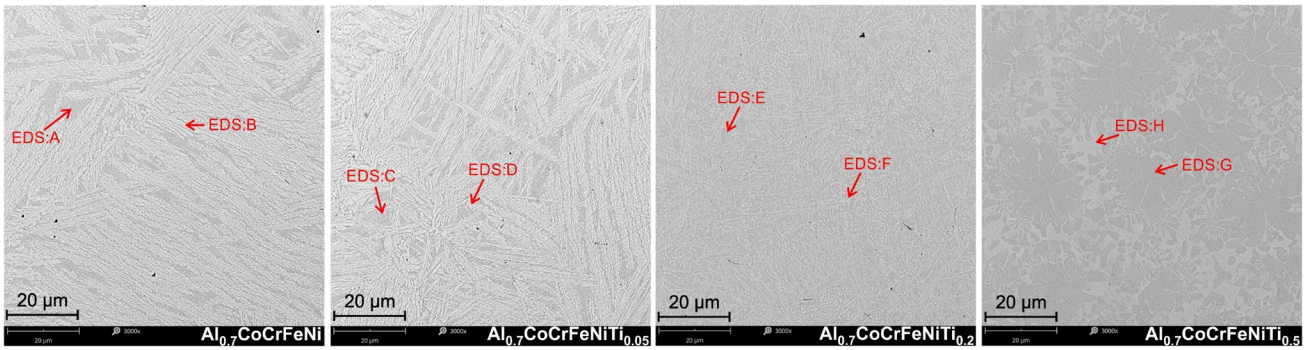


Fig. 3 SEM (BSE) micrographs of the as-cast $Al_{0.7}CoCrFeNiTi_x$ (x = 0, 0.05, 0.2, 0.5) alloys showing the evolution of microstructure with increasing Ti content. Points A–H denote the characteristic microstructural regions analyzed by EDS

Table 4 Results of EDS point analysis (at.%) performed on the characteristic microstructural regions indicated in Fig. 3 for the as-cast $Al_{0.7}CoCrFeNiTi_x$ alloys

Sample	Spot	Al	Co	Cr	Fe	Ni	Ti
$Al_{0.7}CoCrFeNi$	A	15.50	20.45	21.78	21.81	20.46	–
	B	11.39	22.23	21.05	23.51	21.83	–
$Al_{0.7}CoCrFeNiTi_{0.05}$	C	14.51	21.18	22.06	20.88	20.21	1.15
	D	10.62	22.76	21.36	22.87	21.49	0.91
$Al_{0.7}CoCrFeNiTi_{0.2}$	E	13.70	20.05	20.62	20.61	20.79	4.23
	F	8.33	22.10	21.23	24.43	20.87	3.05
$Al_{0.7}CoCrFeNiTi_{0.5}$	G	15.62	19.81	13.93	17.21	24.02	9.41
	H	5.84	19.71	22.54	27.77	18.50	5.63

characteristic microstructural regions marked in the micrographs. The reference $Al_{0.7}CoCrFeNi$ alloy exhibits a well-developed lamellar/needle-like microstructure with a typical Widmanstätten morphology. The structure consists of fine interwoven plates forming a two-constituent arrangement characteristic of arc-melted $Al_xCoCrFeNi$ alloys within the compositional range $0.5 \leq x \leq 0.9$, which is consistent with previously reported Widmanstätten-type morphologies observed in similarly processed $Al_{0.7}CoCrFeNi$ alloys [29]. The BSE contrast clearly indicates the presence of two chemically distinct microstructural constituents. EDS results (Table 4) reveal compositional differences between regions A and B. Region A is relatively enriched in Al (15.50 at.%) with nearly equiatomic contents of Co, Cr, Fe and Ni, whereas region B is depleted in Al (11.39 at.%) and enriched in Fe (23.51 at.%) and Ni (21.83 at.%). These findings indicate chemical partitioning between an Al-enriched constituent and a Fe–Co–Ni-enriched constituent. In combination with XRD results confirming the coexistence of FCC and B2/BCC phases, the Al-enriched constituent can be associated with the B2/BCC phase, while the Fe–Co–Ni-rich constituent corresponds predominantly to the FCC phase. The degree of chemical segregation remains moderate, and the microstructure appears relatively homogeneous at the micrometer scale.

The addition of Ti0.05 mol does not significantly alter the overall lamellar Widmanstätten morphology. However, the BSE contrast becomes more pronounced, indicating intensified chemical partitioning between the coexisting constituents. According to the EDS data, region C contains 14.51 at.% Al and 1.15 at.% Ti, whereas region D is characterized by lower Al (10.62 at.%) and Ti (0.91 at.%) contents together with an increased Fe concentration (22.87 at.%). These results suggest that Ti co-segregates with Al and preferentially partitions into the Al-rich constituent. Consistent with XRD analysis indicating an increased fraction of the B2/BCC phase, the SEM observations confirm enhanced separation between the Al-Ti -rich and Fe-Cr-Co-Ni -rich constituents. Thus, the Ti0.05 addition promotes stabilization of the B2 phase while preserving the overall Widmanstätten-type morphology. For Ti0.2 mol, the microstructure becomes noticeably refined. The lamellar features appear shorter and less regular, and the BSE images reveal greater chemical heterogeneity than in alloys with lower Ti content. EDS analysis

shows significant compositional partitioning between regions E and F. Region E contains 13.70 at.% Al and 4.23 at.% Ti, whereas region F is markedly depleted in Al (8.33 at.%) and Ti (3.05 at.%) and enriched in Fe (24.43 at.%). This confirms progressive separation between the Al-Ti -rich constituent and the Fe-Cr-rich constituent. In agreement with the XRD results, which show an increased BCC fraction and a reduced contribution of the ordered B2 phase, the microstructure can be interpreted as evolving from an FCC-dominant dual-phase system toward a BCC-dominated multiphase structure. The refinement of microstructural features is consistent with increased lattice distortion and reduced crystallite size. The alloy containing Ti0.5 mol exhibits a fundamentally different microstructure. The classical Widmanstätten morphology disappears, replaced by a fine, irregular, interpenetrating multiphase structure with strong BSE contrast, indicating substantial chemical heterogeneity. EDS results for the $Al_{0.7}CoCrFeNiTi_{0.5}$ alloy reveal pronounced compositional partitioning between the characteristic microstructural regions G and H. Region G is enriched in Al, Ti and Ni (15.62, 9.41 and 24.02 at.%, respectively) and relatively depleted in Cr. In contrast, region H is strongly enriched in Fe (27.77 at.%) and Cr (22.54 at.%) and markedly depleted in Al (5.84 at.%). When correlated with XRD results confirming the coexistence of FCC, BCC, Ni_3Ti and σ phases, these findings indicate that the microstructure is no longer a simple dual-phase system but a complex multiphase structure. Based on the combined XRD and SEM/EDS results, the observed chemical partitioning is consistent with the presence of Al–Ti–Ni-rich and Fe–Cr-rich constituents. However, direct assignment of specific phases to the individual SEM-observed regions was not possible within the scope of the present study. Although the morphology may be described as eutectic-like due to the fine, interpenetrating arrangement of the constituents, the confirmed multiphase constitution suggests that it results from complex, coupled solidification involving several phases rather than a classical binary eutectic reaction. The SEM–EDS elemental maps of Ti-modified $Al_{0.7}CoCrFeNi$ alloys were previously reported in our earlier study [25]. In the present work, the XRD results complement the SEM/EDS observations by providing information on the overall phase constitution and its evolution with Ti addition, while remaining consistent with the previously reported elemental distribution.

In summary, the microstructural analysis indicates that increasing Ti content leads to a systematic evolution of the alloy structure. The addition of Ti progressively enhances chemical partitioning between the Al-Ti -rich and Fe-Cr -rich constituents, while simultaneously increasing the fraction of the BCC phase at the expense of the FCC phase. Consequently, the regular Widmanstätten-type morphology gradually transforms into a refined, fine lamellar multiphase interpenetrating structure. At the highest Ti0.5 content, the formation of intermetallic phases, such as Ni_3Ti and σ, becomes clearly evident. Overall, these findings demonstrate that Ti significantly modifies the solidification pathway, promotes BCC stabilization, and stimulates intermetallic phase formation, thereby increasing chemical heterogeneity and the structural complexity of the as-cast alloys.

3.2 Mechanical properties

The surface hardness results presented in Fig. 4 clearly demonstrate a systematic increase in hardness with increasing Ti content in the $Al_{0.7}CoCrFeNiTi_x$ alloys. The reference material, AISI 304L, exhibited an average hardness of approximately 271 HV_1. The base HEA alloy $Al_{0.7}CoCrFeNi$ showed a higher hardness (~347 HV1), about 28% higher than that of the austenitic stainless steel. The introduction of a small amount of Ti0.05 did not result in a significant change in hardness (approximately 352 HV_1), indicating that at such a low addition level the strengthening effect remains limited at the microindentation scale. A pronounced increase in hardness was observed for the Ti0.2 (~461 HV_1) and Ti0.5 (~592 HV_1) alloys. In comparison with the base HEA alloy, this represents an increase of approximately 33% and 71%, respectively, whereas relative to AISI 304L the increase amounts to about 70% and 118%, respectively. The substantial enhancement of surface hardness at higher Ti contents is consistent with the observed microstructural evolution and phase constitution changes. The increasing fraction of the BCC phase at the expense of FCC, and, at the highest Ti content, the presence of intermetallic phases such as Ni_3Ti and σ, contribute to improved resistance to localized plastic deformation. In addition, solid-solution strengthening associated with Ti incorporation, as well as increased chemical heterogeneity of the microstructure, play a significant role in the overall strengthening of the alloys.

 https://doi.org/10.1007/s43452-026-01626-y

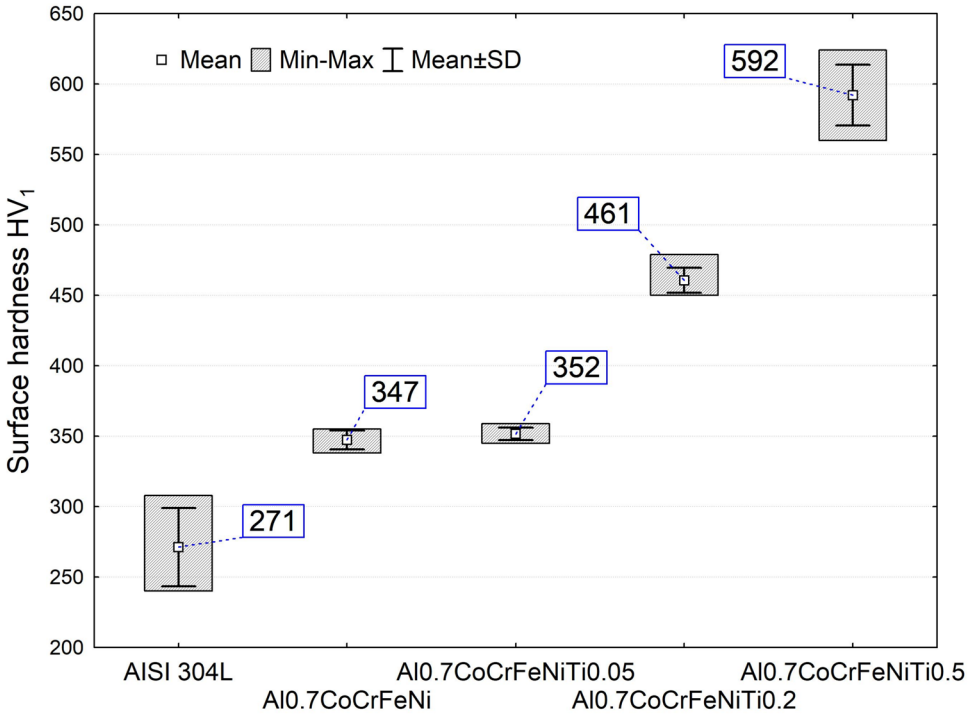


Fig. 4 Vickers microhardness (HV_1) of AISI 304L and $Al_{0.7}CoCrFeNiTi_x$ alloys as a function of Ti content

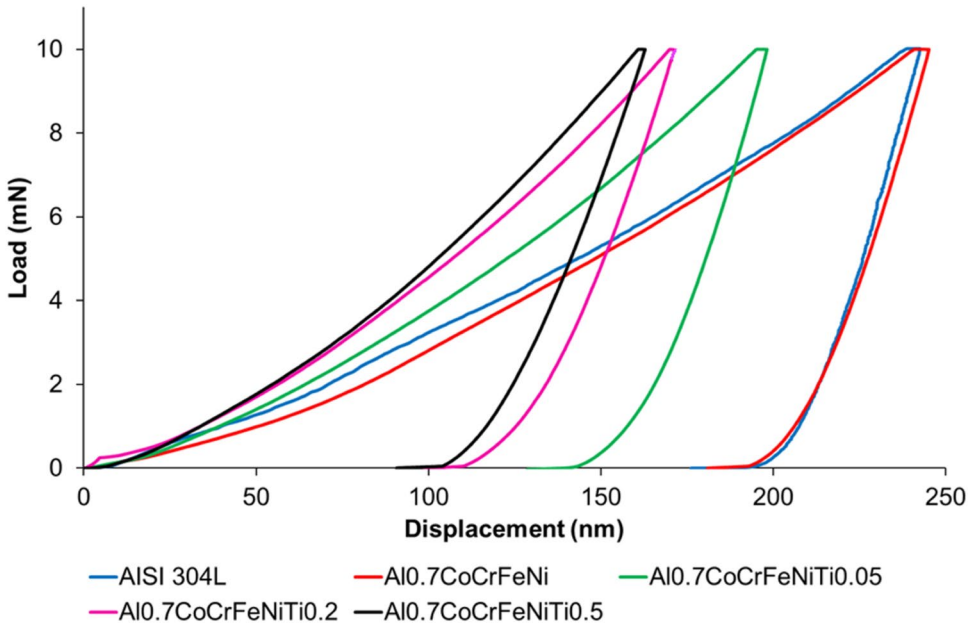


Fig. 5 Representative nanoindentation load–displacement curves obtained for AISI 304L and $Al_{0.7}CoCrFeNiTi_x$ alloys

The representative load–displacement (loading–unloading) curves obtained from nanoindentation tests performed according to the Oliver–Pharr method are presented in Fig. 5, while the corresponding mechanical parameters derived from the analysis are summarized in Table 5. The nanoindentation results confirm the observed trend of increasing mechanical resistance with rising Ti content, with the effect being even more pronounced at the nanoscale than in the HV_1 measurements. The nanohardness H increases from 4.60 GPa for $Al_{0.7}CoCrFeNi$ to 10.4 GPa for $Al_{0.7}CoCrFeNiTi_{0.5}$, corresponding to more than a twofold increase in resistance to indenter penetration. For Ti0.05 and Ti0.2, hardness values of 6.43 GPa and 8.75 GPa were obtained, respectively, indicating systematic strengthening of the material with increasing Ti addition. The elastic modulus E increases from

Table 5 Nanoindentation parameters of AISI 304L and $Al_{0.7}CoCrFeNiTi_x$ alloys

Material	*H* (GPa)	*E* (GPa)	*H*/*E*	H^3/E^2 ($\times 10^{-3}$)	W_{elast} (pJ)	W_{plast} (pJ)	W_{total} (pJ)	Index *ERI*	Index *PI*
AISI 304L	4.84±0.34	228.3±24.3	0.022	2.37	181.2±11.7	864.4±33.5	1046.4±33.2	0.17	0.82
$Al_{0.7}CoCrFeNi$	4.6±0.41	195.2±19.8	0.024	2.56	196.3±11.4	831.1±48.6	1027.4±46	0.19	0.81
$Al_{0.7}CoCrFeNiTi_{0.05}$	6.43±0.56	245.6±22.2	0.026	4.41	199.2±13.8	618.8±42.7	818±36.5	0.24	0.76
$Al_{0.7}CoCrFeNiTi_{0.2}$	8.75±0.8	249.2±39.7	0.035	10.78	229.1±13.4	475.4±25.8	704.5±28.2	0.32	0.67
$Al_{0.7}CoCrFeNiTi_{0.5}$	10.4±2.36	250.2±22.9	0.041	17.79	234.1±21.1	423.4±88.8	657.5±71.3	0.35	0.64

approximately 195 GPa for the base HEA alloy to about 250 GPa for the Ti-containing alloys. However, for $x \geq 0.05$ the changes in E become relatively minor. This suggests that Ti addition affects resistance to plastic deformation to a greater extent than the elastic stiffness of the material. From the perspective of wear resistance, the *H*/*E* and H^3/E^2 ratios are particularly significant. The *H*/*E* value increases from 0.024 for the base alloy to 0.041 for Ti0.5, while the H^3/E^2 parameter increases nearly sevenfold (from 2.56×10^{-3} to 17.79×10^{-3}). The increase in these indicators reflects an enhanced resistance to the initiation of plastic deformation under contact loading, as well as an improved ability to sustain applied loads elastically.

The energy analysis of the load–displacement curves further supports this trend. With increasing Ti content, a marked decrease in plastic work W_{plast} is observed (from ~831 pJ for the base alloy to ~423 pJ for Ti0.5), accompanied by an increase in the elastic work contribution W_{elast}. As a result, the elastic recovery index (*ERI*) increases from 0.19 to 0.35, while the plasticity index (*PI*) decreases from 0.81 to 0.64. This indicates that with increasing Ti content the material exhibits a progressively higher fraction of elastic deformation and a reduced susceptibility to permanent deformation at the contact scale. From the standpoint of nanoindentation parameters, the Ti0.5 alloy demonstrates the highest potential wear resistance due to its high hardness, elevated *H*/*E* and H^3/E^2 values, and reduced contribution of plastic deformation. However, it should be emphasized that the actual tribological performance of multiphase alloys depends not only on nanoscale mechanical parameters, but also on microstructural characteristics, phase distribution, and the potential brittleness of intermetallic constituents, which may significantly influence the wear mechanisms under sliding contact conditions.

3.3 Tribological behaviour

3.3.1 Evolution of the coefficient of friction

The evolution of the coefficient of friction (*COF*) recorded during sliding tests in 3.5 wt.% NaCl solution is presented in Fig. 6. All tested materials exhibited a characteristic running-in stage followed by a quasi-steady sliding regime. During the initial stage (first ~200÷300 s), a rapid increase in *COF* was observed for all materials, which can be attributed to the establishment of real contact area and the formation of the initial tribological interface. After the running-in stage, the *COF* stabilized at different levels depending on the alloy composition. The reference AISI 304L steel exhibited an average *COF* of 0.452 ± 0.055. The base HEA alloy $Al_{0.7}CoCrFeNi$ showed the highest friction coefficient (0.501 ± 0.047), indicating relatively stronger adhesive interaction at the sliding interface. The introduction of titanium significantly influenced the friction behavior. The alloy containing Ti0.05 exhibited a reduced *COF* (0.473 ± 0.048), whereas the lowest friction coefficient was obtained for $Al_{0.7}CoCrFeNiTi_{0.2}$ (0.448 ± 0.044), slightly lower than that of AISI 304L. The further increase of Ti content to Ti0.5 resulted in a moderate increase in friction (0.485 ± 0.054) together with larger fluctuations during sliding. The differences in friction stability are particularly visible in the temporal evolution of *COF*. The Ti0.2 alloy exhibited the most stable friction response with relatively small fluctuations, indicating the formation of a stable tribolayer. In contrast, the Ti0.5 alloy showed pronounced oscillations, suggesting repeated formation and removal of tribological films or brittle fragments generated during sliding. These results indicate that although the addition of Ti generally increases hardness and resistance to plastic deformation, excessive Ti content may

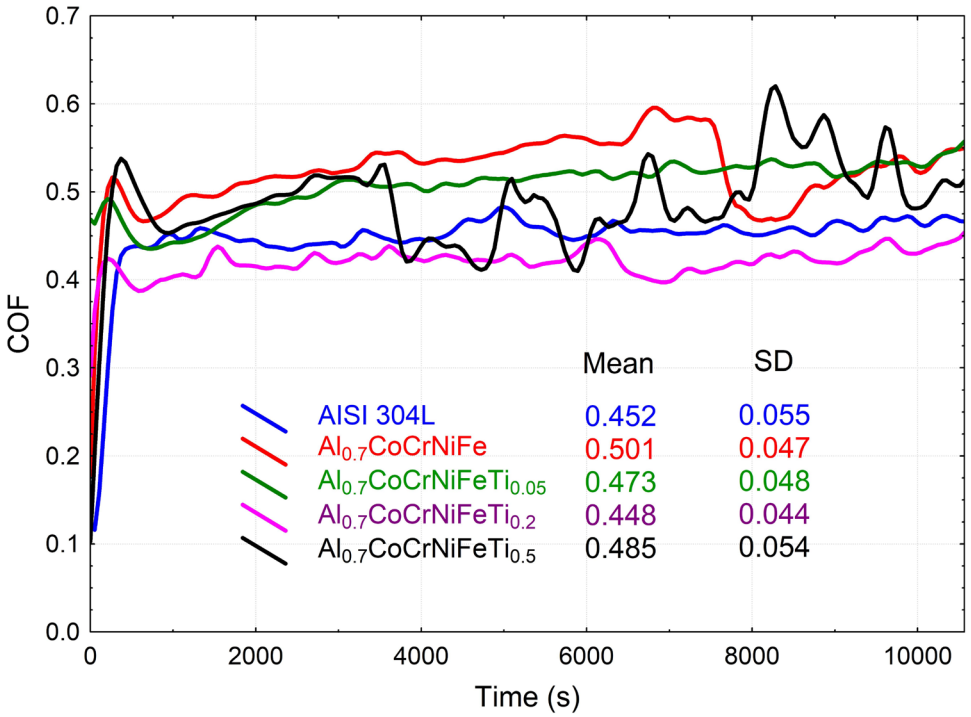


Fig. 6 Evolution of the coefficient of friction (COF) during sliding tests in 3.5 wt.% NaCl solution for AISI 304L and $Al_{0.7}CoCrFeNiTi_x$ alloys

lead to unstable friction conditions due to the formation of brittle intermetallic phases (Ni_3Ti and σ) previously identified in the microstructural analysis.

3.3.2 Wear factor

The wear resistance of the investigated materials was evaluated using the wear factor *K*, and the results are presented in Fig. 7. The AISI 304L steel exhibited the highest wear factor of 6.36×10^{-6} mm^3N^{-1} m^{-1}, indicating relatively low wear resistance under sliding conditions in an aqueous NaCl environment. In comparison, the base HEA alloy $Al_{0.7}CoCrFeNi$ showed a slightly lower wear factor (5.80×10^{-6} mm^3N^{-1} m^{-1}), which can be attributed to its higher hardness and the presence of the strengthening BCC/B2 phase, increasing resistance to local plastic deformation in the contact zone. A significant improvement in wear resistance was observed after introducing Ti. For $Al_{0.7}CoCrFeNiTi_{0.05}$, the wear factor decreased to 3.27×10^{-6} mm^3N^{-1} m^{-1}, while $Al_{0.7}CoCrFeNiTi_{0.2}$ exhibited the lowest value of 2.64×10^{-6} mm^3N^{-1} m^{-1}, corresponding to a reduction of about 58% compared with AISI 304L. These results indicate that a moderate Ti addition significantly improves the tribological performance of the HEA. For the $Al_{0.7}CoCrFeNiTi_{0.5}$ alloy, the wear factor increased slightly to 3.93×10^{-6} mm^3N^{-1} m^{-1}, although it remained considerably lower than that of the reference material. Thus, the best wear resistance was obtained for $Al_{0.7}CoCrFeNiTi_{0.2}$, while further increasing Ti content did not lead to additional improvement. The improved wear resistance of Ti-containing alloys can be partially correlated with nanoindentation results showing increased hardness and higher H/E and H^3/E^2 ratios. These parameters are commonly associated with resistance to the initiation of plastic deformation and improved load-bearing capacity of the surface under contact loading, which reduces asperity penetration and limits material removal. However, despite exhibiting the highest H/E and H^3/E^2 values, the Ti0.5 alloy shows slightly higher wear than Ti0.2. This indicates that resistance to plastic deformation alone does not fully determine the tribological behavior of the investigated HEAs. At higher Ti content, additional intermetallic phases (Ni_3Ti and σ) appear in the microstructure, increasing structural heterogeneity and promoting the formation of harder wear debris acting as third-body abrasive particles. This interpretation is consistent with the wear track morphology discussed in the following section, where the Ti0.2 alloy is characterized

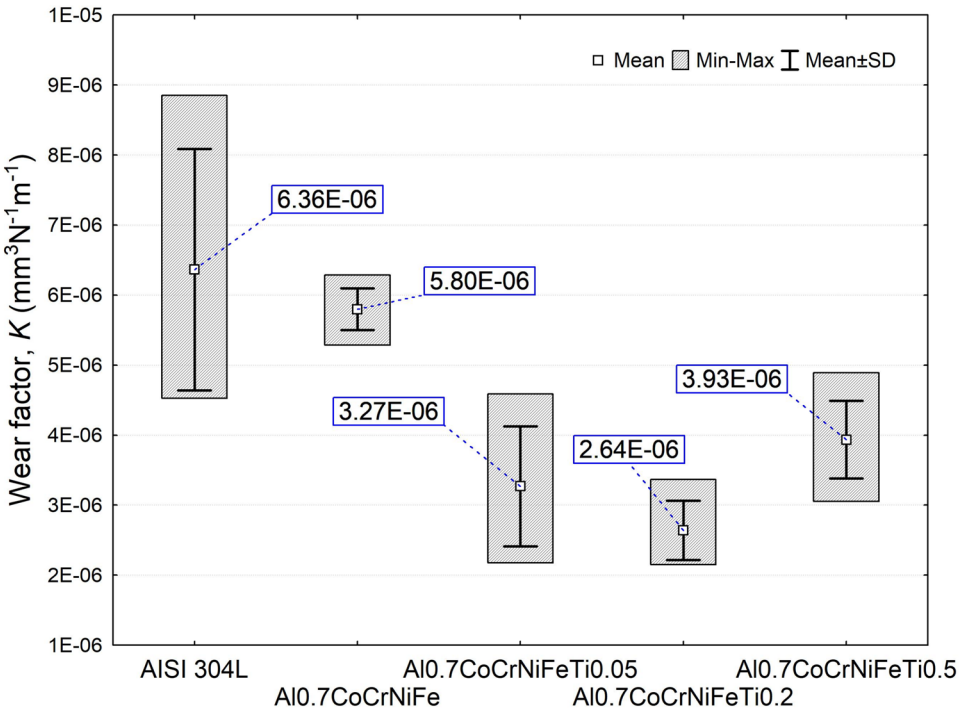


Fig. 7 Wear factor of AISI 304L and $Al_{0.7}CoCrFeNiTi_x$ alloys determined from ball-on-disc tests in 3.5 wt.% NaCl solution

mainly by fine scratches, whereas the Ti0.5 alloy exhibits more pronounced parallel grooving, indicating a more intensive abrasive wear mechanism.

3.3.3 Wear track cross-section profiles

Representative cross-sectional profiles of the wear tracks are presented in Fig. 8. The analysis of the profiles revealed clear differences in both the depth and morphology of the wear tracks depending on the alloy composition. The deepest wear track was observed for AISI 304L, where the maximum wear depth reached approximately 3.8÷4.0 µm, indicating significant material removal during sliding. The wear track profile exhibited a relatively smooth, parabolic shape characteristic of pronounced plastic deformation of the material. The base HEA alloy $Al_{0.7}CoCrFeNi$ showed slightly shallower wear tracks. However, noticeable irregularities were still present, suggesting the contribution of both abrasive and adhesive wear mechanisms. A substantial reduction in wear depth was observed for Ti-containing alloys. The Ti0.05 and Ti0.2 alloys exhibited significantly shallower wear tracks (approximately 2 µm). Among them, the Ti0.2 alloy displayed the most uniform wear profile and the lowest wear depth, confirming its superior wear resistance. An additional feature visible in the wear track profiles is the presence of material pile-up along the edges of the wear grooves, indicating plastic displacement of material during sliding. The intensity of this pile-up tends to increase with increasing Ti content and is particularly pronounced for the Ti0.5 alloy. This suggests that although the alloy exhibits higher hardness, part of the deformation energy is accommodated by lateral material flow at the edges of the wear track. For the Ti0.5 alloy, the wear profile is slightly deeper and more irregular than that observed for Ti0.2, and the pile-up ridges along the track edges are more pronounced. This behavior may be associated with higher local contact stresses and more intensive microploughing processes during sliding. Overall, the wear track profiles confirm the quantitative wear results obtained from the wear factor analysis and indicate that the $Al_{0.7}CoCrFeNiTi_{0.2}$ alloy provides the most favorable balance between resistance to penetration and stability of plastic deformation under sliding contact.

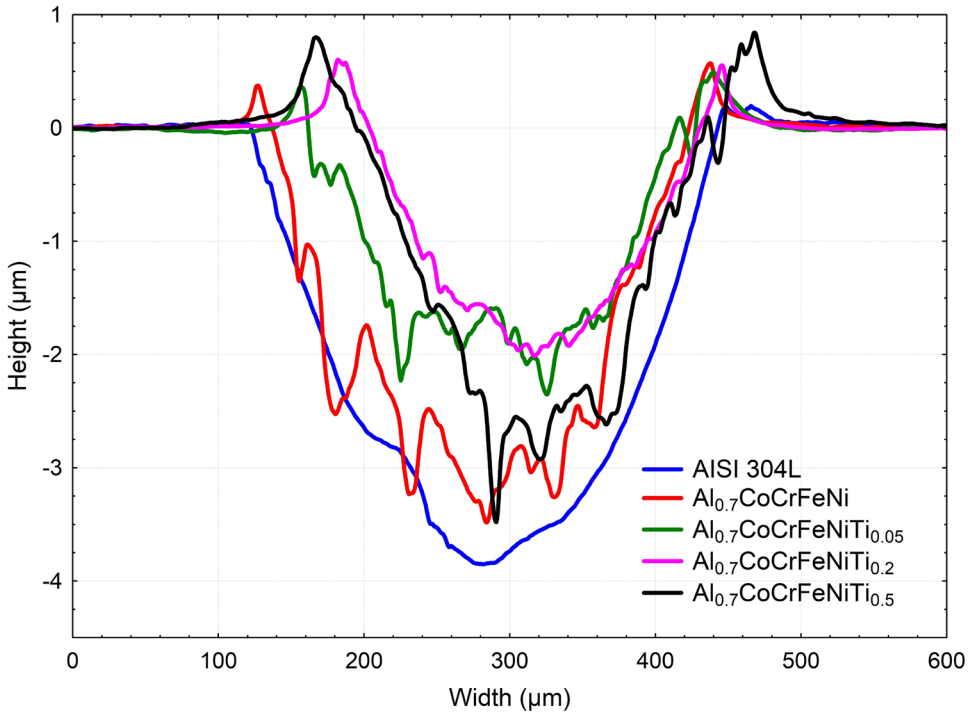


Fig. 8 Representative cross-sectional profiles of wear tracks obtained after sliding tests in 3.5 wt.% NaCl solution. Profiles are representative of measurements performed on three specimens with 12 cross-sections per wear track (N = 36)

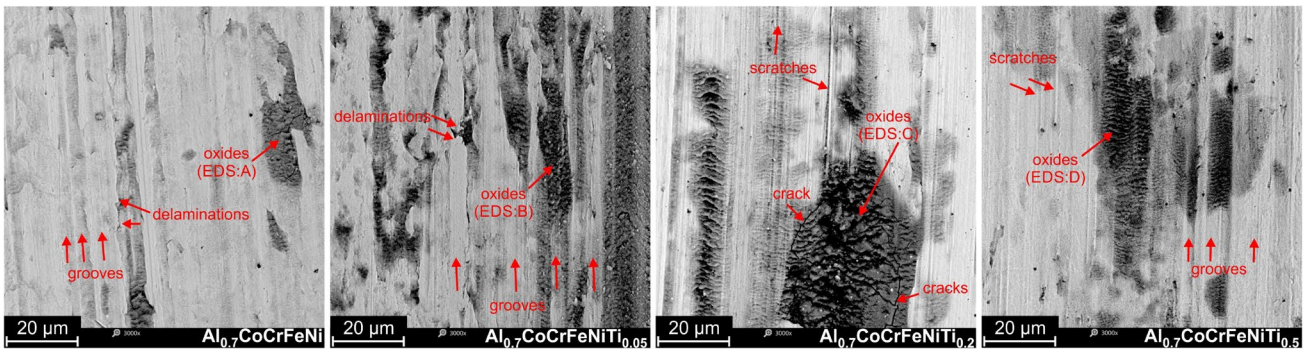


Fig. 9 SEM images of wear tracks on $Al_{0.7}CoCrFeNiTi_x$ alloys after sliding tests in 3.5 wt.% NaCl. EDS analysis points are indicated,—results are given in Table 6

Table 6 EDS point analysis (at.%) of wear track regions formed during sliding tests in 3.5 wt.% NaCl solution

Sample	Spot	O	Al	Co	Cr	Fe	Ni	Ti
$Al_{0.7}CoCrFeNi$	A	44.10	7.62	13.49	11.08	11.86	11.85	–
$Al_{0.7}CoCrFeNiTi_{0.05}$	B	47.25	7.09	12.66	10.73	10.87	10.88	0.53
$Al_{0.7}CoCrFeNiTi_{0.2}$	C	39.57	6.82	13.00	12.57	13.32	12.17	2.54
$Al_{0.7}CoCrFeNiTi_{0.5}$	D	49.67	6.35	10.28	7.98	8.71	10.85	6.15

3.3.4 Morphology of wear tracks and wear mechanisms

The morphology of the wear tracks was analyzed using SEM–EDS. Representative images are presented in Fig. 9, while the EDS results documenting oxidation processes are summarized in Table 6. The observations revealed clear differences in the character of surface damage depending on the composition of the investigated HEA alloys. The worn surface of the base alloy $Al_{0.7}CoCrFeNi$ is characterized by the presence of irregular

grooves and scratches oriented along the sliding direction. In addition to abrasive features, delamination areas are also observed, indicating local detachment of surface layers caused by plastic deformation occurring in the near-surface region. This mechanism is typical for materials exhibiting relatively higher susceptibility to plastic deformation under sliding conditions. A similar wear morphology was observed for the $Al_{0.7}CoCrFeNiTi_{0.05}$ alloy, where, in addition to scratches and grooves generated by abrasive particles, local delamination areas are also present. At the same time, oxidation products formed during sliding in the aqueous environment are visible on the wear track surface, which may accumulate within the contact zone. Introducing a higher amount of Ti leads to a change in the wear behavior. In the case of the $Al_{0.7}CoCrFeNiTi_{0.2}$ alloy, the worn surface is dominated by numerous relatively shallow scratches aligned with the sliding direction. This morphology indicates the predominance of a mild abrasive wear mechanism associated mainly with micro-cutting and micro-ploughing processes caused by fine particles present in the contact zone. Locally observed oxidation products may form thin tribological layers that limit the direct metal-counterbody contact. For the $Al_{0.7}CoCrFeNiTi_{0.5}$ alloy, more pronounced parallel grooving is observed. These grooves are deeper and more regular than the scratches observed for the Ti0.2 alloy, indicating a more intensive abrasive wear mechanism. At the same time, numerous oxidation products are present on the wear track surface, which may undergo fragmentation and act as third-body abrasive particles within the contact interface. This interpretation is consistent with the analysis of the cross-sectional wear track profiles, where more pronounced material pile-up along the groove edges was observed for alloys with higher Ti content. This phenomenon indicates intensified micro-ploughing processes, in which the material is displaced to the sides of the sliding path rather than being completely removed. The obtained results indicate that the wear mechanism of the investigated alloys is governed by the combined action of abrasive wear, oxidative wear, and local delamination processes, while the dominant wear mode evolves with increasing Ti content – from delamination-assisted wear in $Al_{0.7}CoCrFeNi$ and Ti0.05, through mild abrasive wear for Ti0.2, to more pronounced surface grooving in the Ti0.5 alloy. Similar wear mechanisms have also been reported for other AlCoCrFeNi-based HEAs modified with Ti. Wu et al. [23] demonstrated that the addition of Ti increases hardness and promotes a transition toward abrasion-dominated wear. Xu et al. [19] reported that Ti improves wear resistance by increasing the resistance of the material to plastic deformation within the contact zone. At the same time, in oxidizing environments the formation of oxide products may play an important role during sliding. As shown by Li et al. [24], oxide products formed during sliding of Ti-containing HEAs may form tribological layers, while their fragmentation can generate abrasive particles influencing the overall wear behavior. Overall, the obtained results indicate that the $Al_{0.7}CoCrFeNiTi_{0.2}$ alloy exhibits the most favorable tribological performance among the investigated materials, characterized by the mildest wear morphology and the lowest degree of surface damage.

Overall, the wear mechanism evolves with increasing Ti content from abrasion accompanied by local delamination in the base alloy and Ti0.05 composition, through mild abrasive wear dominated by fine scratching for Ti0.2, to more pronounced parallel grooving for Ti0.5. In all cases, tribo-oxidation contributes to the formation of oxide debris that may act as third-body particles and influence the overall wear process.

3.3.5 Wear of the counterbody

SEM analysis of the Al_2O_3 ball surfaces after the tribological tests (Fig. 10) revealed the presence of transferred material and tribological layers formed during sliding. Balls sliding against the $Al_{0.7}CoCrFeNi$ and $Al_{0.7}CoCrFeNiTi_{0.05}$ alloys were covered by irregular accumulations of wear debris. EDS analysis indicated a high oxygen content, confirming the presence of oxide wear products formed during sliding in the aqueous environment. In contrast, for alloys containing higher Ti content, namely $Al_{0.7}CoCrFeNiTi_{0.2}$ and $Al_{0.7}CoCrFeNiTi_{0.5}$, a noticeably larger accumulation of wear products was observed on the ball surface, often forming more extended and compact transfer layers. The EDS results indicate that these layers are predominantly oxide-based, suggesting that tribo-oxidation plays an important role in the generation of wear debris, followed by their transport and compaction on the counterbody surface. The increased accumulation of wear products for the Ti0.2 and Ti0.5 alloys does not necessarily indicate higher plasticity of the material but rather suggests a change in the nature of

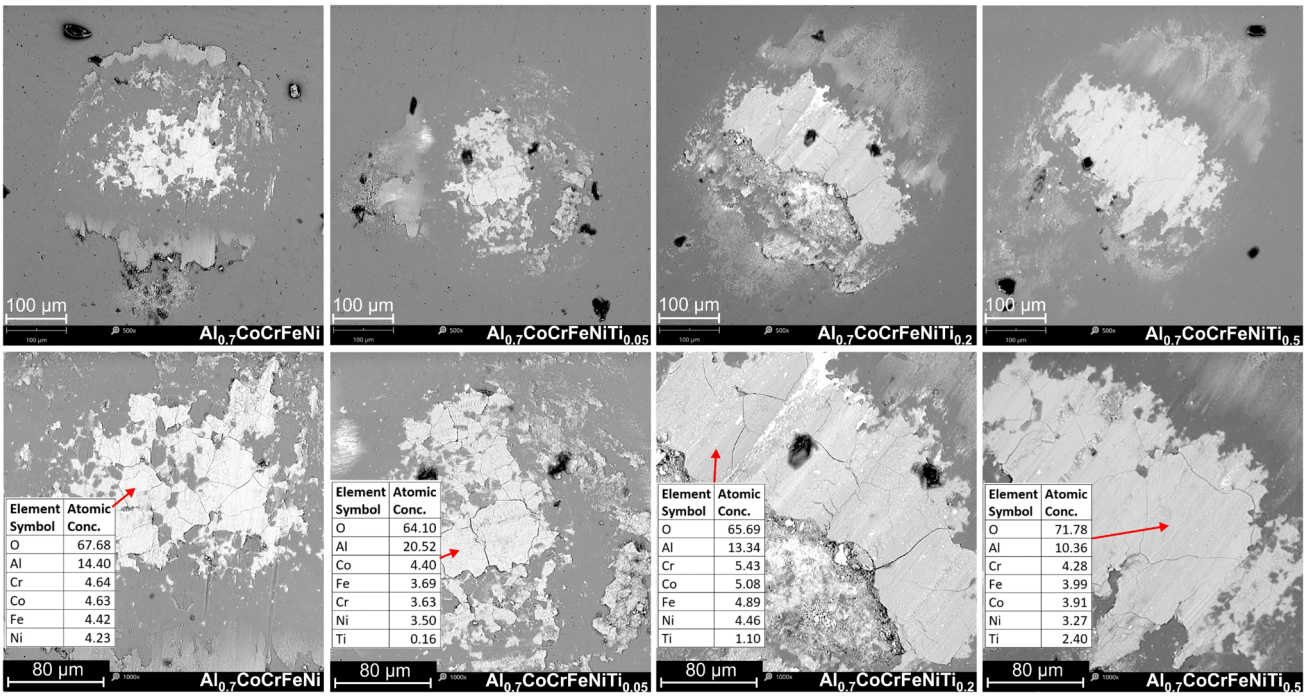


Fig. 10 SEM images of Al_2O_3 counterbody surfaces after sliding tests against $Al_{0.7}CoCrFeNiTi_x$ alloys

the sliding interface. In these cases, the intensified formation of oxide wear debris and their participation in the contact as third-body particles appear to control the tribological interaction. Such transfer layers may intermittently reduce direct metal–ceramic contact. However, depending on their stability and fragmentation, they may also contribute to abrasive interactions within the contact zone.

This observation is consistent with the wear track morphology, where mild scratching dominates for the Ti0.2 alloy, whereas more pronounced parallel grooving is observed for Ti0.5, which may be associated with the different role and stability of oxide particles acting as third-body abrasives.

3.4 Corrosion behavior

The results of the electrochemical polarization tests are presented in the form of Tafel curves in Fig. 11, while the corresponding electrochemical parameters are summarized in Table 7. The potentiodynamic polarization curves indicate that both AISI 304L stainless steel and the investigated HEA alloys undergo passivation in a 3.5 wt.% NaCl environment. However, the stability of the passive film and the susceptibility to its breakdown strongly depend on the titanium content. In the case of the base alloy $Al_{0.7}CoCrFeNi$ and AISI 304L steel, a relatively early transition to a region of rapidly increasing anodic current density can be observed, indicating lower resistance to localized breakdown of the passive layer. The addition of Ti modifies the polarization behavior in a clearly beneficial manner, with the most pronounced effect observed for the $Al_{0.7}CoCrFeNiTi_{0.2}$ alloy, which exhibits the widest range of stable passivation and the highest breakdown potential.

A quantitative analysis of the electrochemical parameters (Table 7) confirms this trend. For the investigated HEA compositions, the addition of Ti results in a systematic decrease in corrosion current density from 1.086 $\mu A \cdot cm^{-2}$ for $Al_{0.7}CoCrFeNi$ to 0.139 $\mu A \cdot cm^{-2}$ for $Al_{0.7}CoCrFeNiTi_{0.5}$, accompanied by a shift of the corrosion potential toward more positive values. For comparison, AISI 304L steel exhibited $i_{corr} = 0.737 \pm 0.043$ $\mu A \cdot cm^{-2}$, which is lower than that of the base HEA alloy. This indicates that even a small addition of Ti improves corrosion resistance in terms of the overall dissolution rate, while larger Ti additions further reduce the electrochemical activity of the alloy. Simultaneously, the corrosion potential E_{corr} shifts toward more noble values, from $-336 \pm$

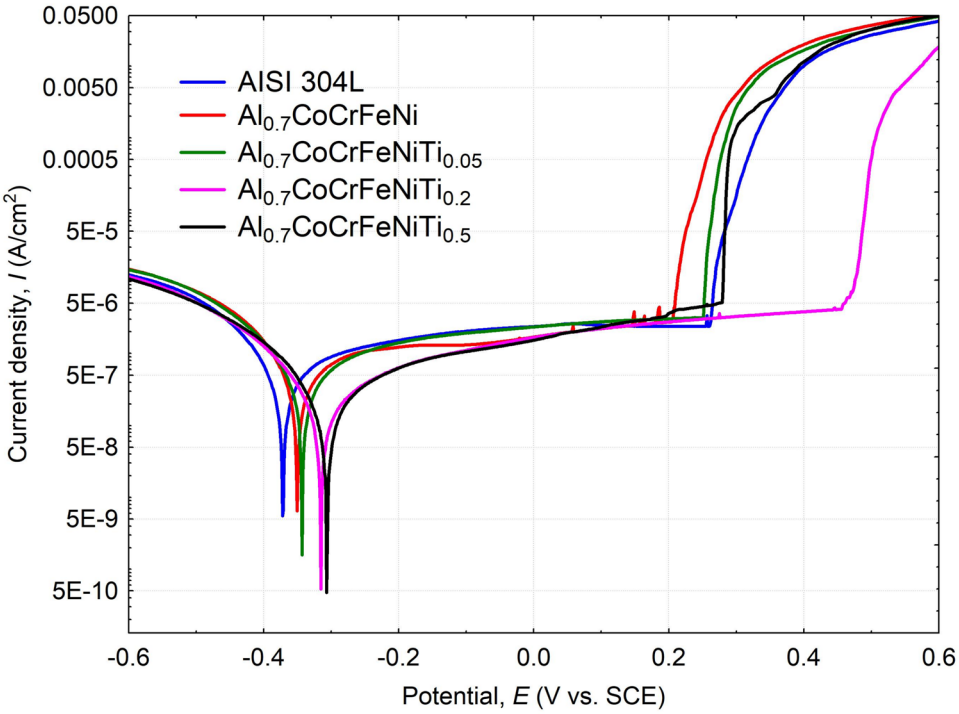


Fig. 11 Potentiodynamic polarization curves of AISI 304L and $Al_{0.7}CoCrFeNiTi_x$ alloys measured in 3.5 wt.% NaCl solution

Table 7 Electrochemical parameters determined from potentiodynamic polarization curves in 3.5 wt.% NaCl solution

Sample	i_{corr} ($\mu A \cdot cm^{-2}$)	E_{corr} (mV)	E_{pit} (mV)
AISI 304L	0.737±0.043	−352±13	255±17
$Al_{0.7}CoCrFeNi$	1.086±0.050	−336±21	204±2
$Al_{0.7}CoCrFeNiTi_{0.05}$	0.654±0.014	−324±26	239±16
$Al_{0.7}CoCrFeNiTi_{0.2}$	0.328±0.019	−318±17	442±37
$Al_{0.7}CoCrFeNiTi_{0.5}$	0.139±0.002	−305±2	263±20

21 mV for the Ti-free alloy to −305 ± 2 mV for the Ti0.5 variant, which also indicates improved electrochemical behavior after Ti addition.

However, the values of i_{corr} and E_{corr} alone do not fully describe resistance to localized corrosion in chloride-containing environments. A key parameter in this context is the pitting potential E_{pit}, which shows a non-linear dependence on Ti content for the investigated alloys. The lowest value was observed for the base $Al_{0.7}CoCrFeNi$ alloy, indicating the highest susceptibility to pit initiation. The addition of 0.05 mol Ti increases the E_{pit} value to a level comparable with that of AISI 304L. The most favorable behavior, however, is exhibited by the $Al_{0.7}CoCrFeNiTi_{0.2}$ alloy, for which E_{pit} reaches 442 ± 37 mV, clearly exceeding the values obtained for the other materials. Further increasing the Ti content to 0.5 mol leads to a reduction of E_{pit} to 263 ± 20 mV. These results clearly indicate that the optimum resistance to passive film breakdown occurs at an intermediate Ti content rather than at the highest Ti concentration.

This apparent discrepancy between decreasing i_{corr} and the maximum E_{pit} observed for Ti0.2 can be explained by correlating the electrochemical results with the phase composition and chemical segregation of the investigated alloys. XRD and SEM analyses show that all $Al_{0.7}CoCrFeNiTi_x$ alloys exhibit a mixed FCC + B2/BCC structure, while increasing Ti content promotes the growth of the BCC/B2 fraction at the expense of the FCC phase. For the Ti0.5 alloy, additional intermetallic phases such as Ni_3Ti and σ are observed, together with significantly stronger chemical segregation between Al–Ti–Ni-rich regions and Fe–Cr-rich regions. Although Ti promotes the formation of more protective passive products, excessive chemical and phase heterogeneity may

simultaneously increase the number of local micro-galvanic couples and potential sites for localized corrosion initiation. Consequently, the Ti0.5 alloy exhibits a very low corrosion current density but does not achieve the same resistance to pitting corrosion as the Ti0.2 alloy.

Chloride-containing environments are particularly aggressive for metallic materials because chloride ions can destabilize passive films and promote pitting corrosion. Under such conditions, localized corrosion often develops in microstructural regions characterized by chemical heterogeneity [30]. SEM observations of the surfaces after corrosion testing (Fig. 12) are consistent with the analysis of the polarization curves. For the base $Al_{0.7}CoCrFeNi$ alloy, local corrosion attack can be observed mainly along the needle-like/lamellar morphological features, together with isolated pits developing within specific microstructural constituents. A similar damage morphology is observed for the alloys in the Ti0÷Ti0.2 range. In contrast, the $Al_{0.7}CoCrFeNiTi_{0.5}$ alloy, characterized by a distinctly different microstructure, exhibits numerous locally etched areas and corrosion attack along the boundaries between microstructural constituents. This behavior can be attributed to the high degree of chemical and phase heterogeneity in this alloy. In this composition, pits tend to nucleate in darker regions (depleted in Cr) located in close proximity to brighter precipitates.

EDS point analysis performed on the corroded surfaces (Table 8) indicates that the areas subjected to stronger electrochemical attack are mainly associated with regions enriched in Al and Ni but depleted in Cr and Fe, or, conversely, with regions exhibiting strong deviations from the average composition where local chemical segregation occurs. In the $Al_{0.7}CoCrFeNi$ alloy, region P3 (located in a non-pitted area), interpreted as a more

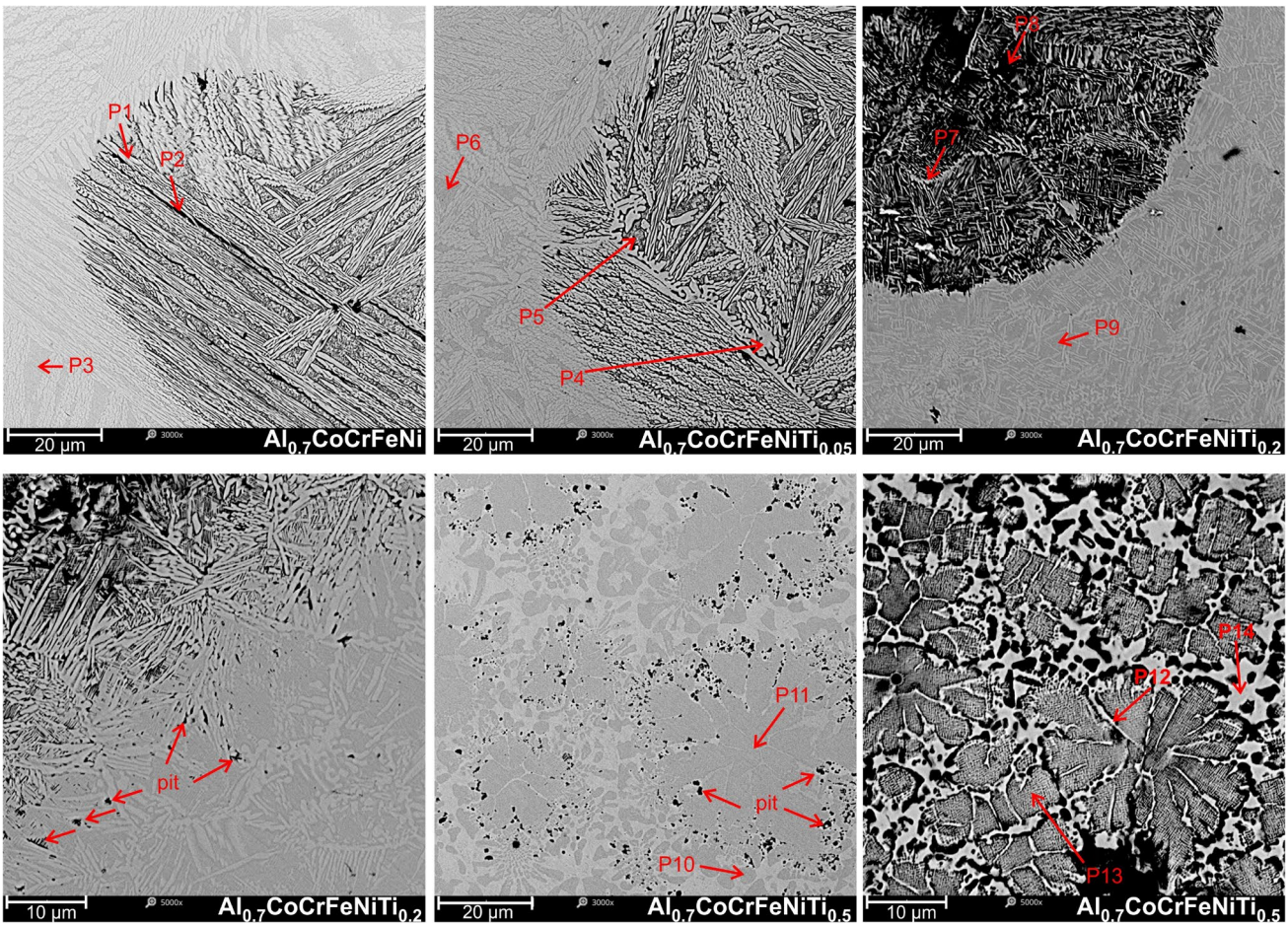


Fig. 12 SEM micrographs of $Al_{0.7}CoCrFeNiTi_x$ alloy surfaces after corrosion tests in 3.5 wt.% NaCl solution. Points indicate locations of EDS analysis; the corresponding chemical composition is given in Table 8

Table 8 EDS point analysis (at.%) of selected regions on corroded surfaces of $Al_{0.7}CoCrFeNiTi_x$ alloys (analysis points indicated in Fig. 12)

Sample	Spot	O	Al	Co	Cr	Fe	Ni	Ti
$Al_{0.7}CoCrFeNi$	P1	13.46	8.39	19.39	20.58	21.18	17.00	–
	P2	9.45	5.55	20.44	26.45	22.90	15.21	–
	P3	17.94	14.09	16.55	17.54	17.11	16.77	–
$Al_{0.7}CoCrFeNiTi_{0.05}$	P4	16.60	7.28	19.46	19.10	20.11	16.83	0.62
	P5	22.74	9.01	16.35	21.97	17.63	11.56	0.74
	P6	17.06	14.01	16.81	17.07	16.67	17.36	1.02
$Al_{0.7}CoCrFeNiTi_{0.2}$	P7	17.80	5.83	17.61	21.37	21.46	14.33	1.60
	P8	24.20	1.88	12.91	33.20	20.82	5.85	1.14
	P9	14.78	10.72	17.66	17.66	17.73	17.73	3.72
$Al_{0.7}CoCrFeNiTi_{0.5}$	P10	14.91	13.42	17.80	8.43	11.00	21.90	12.53
	P11	13.58	14.92	17.19	11.68	14.45	20.29	7.88
	P12	11.19	3.11	15.58	31.03	27.22	9.11	2.38
	P13	20.16	2.57	13.09	29.72	25.31	6.95	2.20
	P14	13.56	3.77	16.79	22.01	26.60	14.06	3.21

homogeneous Al-rich area, contains 14.09 at.% Al and nearly equal fractions of Co, Cr, Fe, and Ni. In contrast, pit regions represented by points P1÷P2 show lower Al content and higher Cr concentration. Similar relationships are observed for the Ti-containing alloys, confirming that localized corrosion preferentially develops at boundaries between chemically distinct microstructural constituents, particularly in areas with elevated Al and Ni content. In the $Al_{0.7}CoCrFeNiTi_{0.5}$ alloy, post-corrosion EDS analysis reveals a pronounced separation between Al–Ti–Ni-rich regions (e.g., P10 and P11) and Cr–Fe-rich regions associated with pit development (P12 and P13). Such compositional separation is consistent with the previously identified multiphase microstructure containing additional intermetallic phases. This type of microstructural architecture promotes local differences in electrochemical activity, which explains why, despite its very low corrosion current density, the Ti0.5 alloy does not reach the same pitting resistance as the Ti0.2 variant.

From the perspective of degradation mechanisms, corrosion in the investigated alloys can therefore be described as a mixed process. The matrix undergoes passivation, while damage initiation occurs locally in micro-regions characterized by unfavorable chemical composition and/or at phase boundaries. In alloys without Ti and with small Ti additions, the presence of Al–Ni-rich regions associated with the B2/BCC phase plays a significant role, as these regions are less resistant in chloride environments due to their lower Cr content. The introduction of a moderate amount of Ti improves passive film stability, probably due to the presence of Ti-containing oxides in the surface film and a more favorable redistribution of phases. Further increasing Ti content, however, leads to excessive microstructural heterogeneity and enhances local galvanic effects.

The obtained results are also consistent with general trends reported in the literature for AlCoCrFeNi-based alloys and their modifications with alloying additions. Shi et al. [8] demonstrated that the corrosion behavior of base $Al_xCoCrFeNi$ alloys in chloride environments is strongly related to the microstructure and the fraction of BCC/B2 phases, which may promote localized corrosion initiation due to chemical heterogeneity within the alloy. A similar role of microstructural changes was emphasized by Yue et al. [21] and Li et al. [24], who showed that alloying additions such as Ti modify both the phase constitution and the nature of the passive film, which may simultaneously improve general corrosion resistance while influencing the susceptibility to localized corrosion processes. Yue et al. [21], investigating equimolar $AlCoCrFeNiTi_x$ coatings produced by laser cladding, demonstrated that the addition of Ti modifies the phase constitution of the coatings from a single BCC phase to a mixed BCC + B2 structure, while at approximately 0.5 mol Ti the formation of a Laves phase was also observed. At the same time, Ti promotes the formation of a protective passive film and limits pit propagation; however, corrosion resistance improves only up to a certain Ti content and then begins to deteriorate. In their system, the optimum corrosion resistance was observed at a Ti content of approximately 0.5 mol. These results are generally consistent

with the trend observed in the present study. We also observe an initial improvement in corrosion resistance after the addition of Ti, followed by a loss of the optimum at higher Ti contents as the microstructural heterogeneity increases. The main difference concerns the position of the optimum. In the present cast alloys, the best pitting resistance (in terms of E_{pit}) was obtained for the Ti0.2 composition rather than Ti0.5. The most probable explanation for this discrepancy is the difference in processing technology and the resulting microstructural architecture. In laser-cladded coatings, rapid solidification usually leads to a finer and more homogeneous microstructure than in cast materials. Therefore, higher Ti contents can be better tolerated without the formation of strongly pronounced micro-galvanic couples. Furthermore, Zhang et al. [22] emphasized that the corrosion resistance of AlCoCrFeNiTi-based HEAs is largely determined by the balance between passive film stability and the chemical heterogeneity of the microstructure. In this context, the results of the present study confirm that the optimum corrosion resistance of the investigated alloys does not depend solely on the content of the alloying addition, but rather on a compromise between improved passivation and the limitation of local compositional differences and electrochemical activity within the microstructure.

Overall, the corrosion test results demonstrate that Ti addition exerts a clearly beneficial influence on the electrochemical behavior of $Al_{0.7}CoCrFeNiTi_x$ alloys in 3.5 wt.% NaCl solution. However, the effect depends on the evaluation criterion. From the perspective of general corrosion resistance, the lowest electrochemical activity is observed for the $Al_{0.7}CoCrFeNiTi_{0.5}$ alloy. In contrast, with respect to resistance to localized corrosion, the best performance is achieved by $Al_{0.7}CoCrFeNiTi_{0.2}$, which exhibits the highest pitting potential and the most stable passive region. These results indicate that in the design of HEA alloys intended for service in chloride-containing environments, the key factor is not only the presence of Ti but primarily maintaining an optimal balance between improved passivation and limited chemical segregation and phase complexity within the microstructure.

4 Conclusions

Alloying $Al_{0.7}CoCrFeNi$ with Tix (x = 0÷0.5) significantly modifies the microstructure and phase constitution, transforming the lamellar/Widmanstätten morphology into a complex multiphase structure with an increasing fraction of BCC/B2 phases, which is reflected in the mechanical, tribological and corrosion behaviour in 3.5 wt.% NaCl solution. Based on the conducted structural, mechanical, tribological and electrochemical investigations of $Al_{0.7}CoCrFeNiTi_x$ alloys, the following conclusions can be drawn:

- The addition of Ti significantly modifies the microstructure of the $Al_{0.7}CoCrFeNi$ alloy, promoting the growth of the BCC/B2 phase at the expense of FCC and enhancing chemical segregation between Al–Ti–rich and Fe–Cr-rich regions. At the highest Ti content (x = 0.5), additional intermetallic phases such as Ni_3Ti and σ were identified.
- Increasing Ti content leads to a substantial improvement in mechanical properties. The nanohardness increases from about 4.6 GPa for the base alloy to approximately 10.4 GPa for Ti0.5, accompanied by higher H/E and H^3/E^2 ratios and increased elastic recovery, indicating enhanced resistance to plastic deformation under contact loading.
- All investigated HEAs exhibit higher wear resistance in 3.5 wt.% NaCl solution compared with AISI 304L stainless steel. The best tribological performance was obtained for $Al_{0.7}CoCrFeNiTi_{0.2}$, whose wear factor was approximately 58% lower than that of AISI 304L and about 54% lower than that of the Ti-free base HEA alloy.
- The wear mechanism evolves with increasing Ti content from abrasion accompanied by local delamination in the base alloy to mild abrasive wear for $Ti_{0.2}$ and more pronounced micro-ploughing for Ti0.5. In all investigated HEA compositions, oxidative wear occurred simultaneously, and oxide debris may act as third-body particles in the sliding interface.
- The addition of Ti improves the overall corrosion resistance of the HEAs in chloride environments by reducing the corrosion current density and shifting the corrosion potential toward more noble values. The highest

resistance to pitting corrosion was observed for $Al_{0.7}CoCrFeNiTi_{0.2}$, which exhibited the highest pitting potential and the most stable passive region.

- Post-corrosion analysis revealed that localized corrosion preferentially develops in microstructural regions enriched in Al and Ni but depleted in Cr, which promotes the formation of local micro-galvanic cells between chemically distinct constituents of the alloy.

From the perspective of potential applications in chloride-containing wet environments, the $Al_{0.7}CoCrFeNiTi_{0.2}$ alloy exhibits the most favorable performance, combining superior wear resistance with the highest resistance to pitting corrosion, thus providing the optimal balance between mechanical, tribological and electrochemical properties.

Acknowledgements This work was partially supported by the commissioned task entitled "VIA CARPATIA Universities of Technology Network named after the President of the Republic of Poland Lech Kaczyński" (contract no. MEiN/2022/DPI/2575), within the ISKRA programme – building inter-university research teams. It was also partially carried out during the research stay of Mariusz Walczak at the Faculty of Military Technology, University of Defence in Brno (24 November–12 December 2025). In addition, the study was partially funded by the "Partial development intention funding" VAROPS.

Data availability The processed data required to reproduce these findings will be made available on reasonable request.

Declarations

Conflict of interest The author states that there is no conflict of interest.

Open Access This article is licensed under a Creative Commons Attribution 4.0 International License, which permits use, sharing, adaptation, distribution and reproduction in any medium or format, as long as you give appropriate credit to the original author(s) and the source, provide a link to the Creative Commons licence, and indicate if changes were made. The images or other third party material in this article are included in the article's Creative Commons licence, unless indicated otherwise in a credit line to the material. If material is not included in the article's Creative Commons licence and your intended use is not permitted by statutory regulation or exceeds the permitted use, you will need to obtain permission directly from the copyright holder. To view a copy of this licence, visit http://creativecommons.org/licenses/by/4.0/.

References

1. Walczak M, Nowak WJ, Okuniewski W, Chocyk D. Effect of adding molybdenum on microstructure, hardness, and corrosion resistance of an AlCoCrFeNiMo0.25 high-entropy alloy. Materials. 2025;18:4566. https://doi.org/10.3390/ma18194566.
2. Zhang M, Zhang Y, Dai P, Zhao L, Wu L, Li S. Study on the process parameters and corrosion resistance of FeCoNiCrAl high entropy alloy coating prepared by atmospheric plasma spraying. Materials (Basel). 2025;18:1396. https://doi.org/10.3390/ma18071396.
3. Liu H, Sun S, Zhang T, Zhang G, Yang H, Hao J. Effect of Si addition on microstructure and wear behavior of AlCoCrFeNi high-entropy alloy coatings prepared by laser cladding. Surf Coat Technol. 2021;405:126522. https://doi.org/10.1016/j.surfcoat.2020.126522.
4. Tokarewicz M, Grądzka-Dahlke M. Review of recent research on AlCoCrFeNi high-entropy alloy. Metals (Basel). 2021;11:1302. https://doi.org/10.3390/met11081302.
5. Liu G, Liu L, Liu X, Wang Z, Han Z, Zhang G, et al. Microstructure and mechanical properties of Al0.7CoCrFeNi high-entropy-alloy prepared by directional solidification. Intermetallics. 2018;93:93–100. https://doi.org/10.1016/j.intermet.2017.11.019.
6. She S, Wang C, Chen M, Ji V. Mechanical properties and strengthening mechanisms of FCC-based and refractory high-entropy alloys: a review. Metals (Basel). 2025;15:247. https://doi.org/10.3390/met15030247.
7. Geanta V, Voiculescu I, Milosan I, Istrate B, Mates IM. Chemical composition influence on microhardness, microstructure and phase morphology of AlxCrFeCoNi high entropy alloys. Rev Chim. 2018;69:798–801. https://doi.org/10.37358/RC.18.4.6203.
8. Shi Y, Yang B, Xie X, Brechtl J, Dahmen KA, Liaw PK. Corrosion of Al_xCoCrFeNi high-entropy alloys: Al-content and potential scan-rate dependent pitting behavior. Corros Sci. 2017;119:33–45. https://doi.org/10.1016/j.corsci.2017.02.019.

9. Kao Y-F, Lee T-D, Chen S-K, Chang Y-S. Electrochemical passive properties of AlxCoCrFeNi (x=0, 0.25, 0.50, 1.00) alloys in sulfuric acids. Corros Sci. 2010;52:1026–34. https://doi.org/10.1016/j.corsci.2009.11.028.
10. Rakesh B, Nair HS, Arora AV, Boyana P, Saiteja HS. Tribological behavior of microwave synthesized high entropy alloy claddings. Wear. 2019. https://doi.org/10.1016/j.wear.2019.203028.
11. Nie S, Zheng Z, Qiao Y, Duan Y, Cui J, Mekkey SD, et al. Corrosion behavior of as-cast Al0.75CoCr1.25FeNi high entropy alloy in 0.5 mol/L sulfuric acid. Adv Compos Hybrid Mater. 2024;7:138. https://doi.org/10.1007/s42114-024-00951-1.
12. Ma SG, Zhang Y. Effect of Nb addition on the microstructure and properties of AlCoCrFeNi high-entropy alloy. Mater Sci Eng, A. 2012;532:480–6. https://doi.org/10.1016/j.msea.2011.10.110.
13. Tokarewicz M, Gradzka-Dahlke M, Nowak WJ, Gradzik A, Szala M, Walczak M. Effect of vanadium addition on the wear resistance of Al0.7CoCrFeNi high-entropy alloy. Materials (Basel). 2024;17:6021. https://doi.org/10.3390/ma17236021.
14. Qiushi C, Yong D, Junjia Z, Yiping L. Microstructure and properties of AlCoCrFeNiB x (x =0, 0.1, 0.25, 0.5, 0.75, 1.0) high entropy alloys. Rare Metal Mater Eng. 2017;46:651–6. https://doi.org/10.1016/S1875-5372(17)30112-1.
15. Chen J, Niu P, Liu Y, Lu Y, Wang X, Peng Y, et al. Effect of Zr content on microstructure and mechanical properties of AlCoCrFeNi high entropy alloy. Mater Des. 2016;94:39–44. https://doi.org/10.1016/j.matdes.2016.01.033.
16. Hassan MA, Yehia HM, Mohamed ASA, El-Nikhaily AE, Elkady OA. Effect of copper addition on the AlCoCrFeNi high entropy alloys properties via the electroless plating and powder metallurgy technique. Crystals. 2021;11:540. https://doi.org/10.3390/cryst11050540.
17. Zhang D, Li Q, Sun R, Chang C, Liu B, Ma X. Effect of Mn addition on microstructure and corrosion behavior of AlCoCrFeNi high-entropy alloy. Intermetallics. 2024;167:108236. https://doi.org/10.1016/j.intermet.2024.108236.
18. Walczak M, Nowak WJ, Szala M, Grądzka-Dahlke M, Maciaszek N, Vališ D, et al. Effect of molybdenum addition on microstructure and behavior of AlCoCrFeNi high-entropy alloys in wet environments. Arch Civ Mech Eng. 2025;25:205. https://doi.org/10.1007/s43452-025-01260-0.
19. Xu Z, Li DY, Chen DL. Effect of Ti on the wear behavior of AlCoCrFeNi high-entropy alloy during unidirectional and bi-directional sliding wear processes. Wear. 2021;476:203650. https://doi.org/10.1016/j.wear.2021.203650.
20. Olejarz A, Huo W, Kalita D, Zieliński M, Wyszkowska E, Chromiński W, et al. Cr-rich structure evolution and enhanced mechanical properties of CoCrFeNi high entropy alloys by mechanical alloying. J Mater Res Technol. 2024;30:1490–504. https://doi.org/10.1016/j.jmrt.2024.03.116.
21. Yue K, Wang L, Xu Z, Cheng C, Wang Y, Fan Y, et al. Effect of Ti addition on the microstructure and corrosion behavior of laser cladding AlCoCrFeNi high-entropy alloy coatings. Vacuum. 2024;230:113633. https://doi.org/10.1016/j.vacuum.2024.113633.
22. Zhang JJ, Yin XL, Dong Y, Lu YP, Jiang L, Wang TM, et al. Corrosion properties of $Al_xCoCrFeNiTi_{0.5}$ high entropy alloys in 0·5M H_2SO_4 aqueous solution. Mater Res Innov. 2014;18:S4-756-S4-760. https://doi.org/10.1179/1432891714Z.000000000778.
23. Wu M, Chen K, Xu Z, Li DY. Effect of Ti addition on the sliding wear behavior of AlCrFeCoNi high-entropy alloy. Wear. 2020;462–463:203493. https://doi.org/10.1016/j.wear.2020.203493.
24. Li Z, Mei K, Dong J, Yang Y, Sun J, Luo Z. An investigation on the wear and corrosion resistance of AlCoCrFeNi high-entropy alloy coatings enhanced by Ti and Si. Surf Coat Technol. 2024;487:130949. https://doi.org/10.1016/j.surfcoat.2024.130949.
25. Nowak WJ, Kubaszek T, Gradzik A, Grądzka-Dahlke M, Perkowski D, Tokarewicz M, et al. Effect of Ti doping of Al0.7CoCrFeNi-based high entropy alloys on their erosion resistance by solid particles. Materials (Basel). 2025;18:3328. https://doi.org/10.3390/ma18143328.
26. Oliver WC, Pharr GM. Measurement of hardness and elastic modulus by instrumented indentation: advances in understanding and refinements to methodology. J Mater Res. 2004;19:3–20. https://doi.org/10.1557/jmr.2004.19.1.3.
27. PN-EN ISO 14577–1:2015: Metallic materials - Instrumented indentation test for hardness and materials parameters - Part 1: Test method, (n.d.).
28. Archard JF. Contact and rubbing of flat surfaces. J Appl Phys. 1953;24:981–8. https://doi.org/10.1063/1.1721448.
29. De Jeer LTH, Ocelík V, De Hosson JTM. Orientation relationships in $Al_{0.7}$ CoCrFeNi high-entropy alloy. Microsc Microanal. 2017;23:905–15. https://doi.org/10.1017/S1431927617012442.
30. Lachowicz MM. Metallurgical aspects of the corrosion resistance of 7000 series aluminum alloys – a review. Mater Sci-Poland. 2023;41:159–80. https://doi.org/10.2478/msp-2023-0041.

Publisher's Note Springer Nature remains neutral with regard to jurisdictional claims in published maps and institutional affiliations.

Authors and Affiliations

Mariusz Walczak[1] · Wojciech J. Nowak[2] · David Vališ[3] · Wojciech Okuniewski[1] · Dariusz Chocyk[1] · Kamil Pasierbiewicz[4]

✉ Mariusz Walczak
m.walczak@pollub.pl

Wojciech J. Nowak
w.nowak@prz.edu.pl

David Vališ
david.valis@unob.cz

Wojciech Okuniewski
w.okuniewski@pollub.pl

Dariusz Chocyk
d.chocyk@pollub.pl

Kamil Pasierbiewicz
kamil.pasierbiewicz@wsei.lublin.pl

[1] Faculty of Mechanical Engineering, Lublin University of Technology, Nadbystrzycka 36D, 20-618 Lublin, Poland

[2] Faculty of Mechanical Engineering and Aeronautics, Rzeszow University of Technology, Powstanców Warszawy 12, 35-959 Rzeszów, Poland

[3] Faculty of Military Technologies, University of Defence, Kounicova 65. 662-10, Brno, Czech Republic

[4] Faculty of Transport and Computer Science, WSEI University in Lublin, Projektowa 4, 20-209 Lublin, Poland